A nondimensional model of droplet ejection for drop-on-demand inkjet printing

James Q. Feng

OXCBO Research, Maple Grove, Minnesota, USA

E-mail: james.q.feng@gmail.com

Abstract

A nondimensional model is established within the framework of the OpenFOAM® volume-of-fluid (VOF) method for computational fluid dynamics (CFD). In terms of the Reynolds number Re and capillary number Ca, which explicitly appear in the nondimensional VOF version of the Navier-Stokes equations, another dimensionless parameter $Z = \sqrt{Re/Ca}$ can be derived to characterize the ink properties (for a given nozzle size), and $Re/Z = \sqrt{Re\,Ca}$ to serve as the nondimensional actuation strength. Most of the fundamental behavior of droplet ejection in drop-on-demand (DOD) inkjet printing appears to be controlled by Z and Re/Z, as noted by many previous authors. But the boundaries of the operational window in a Re/Z versus Z diagram are shown to change when the nondimensional actuation pulse width $\Delta\tilde{\tau}$ (which determines the relative droplet size with respect to the nozzle size) is changed—a fact less discussed in the literature. By reducing $\Delta\tilde{\tau}$, the possibility of generating droplets of sizes smaller than a given nozzle size is systematically studied herewith. Moreover, the effect of the ink wetting property on the wall of the nozzle orifice is also briefly examined. Such a nondimensional model analysis could provide fresh insights into the complex droplet ejection behavior in DOD inkjet printing.

Keywords: Droplet ejection, drop-on-demand inkjet, volume-of-fluid computation, dimensionless parameters

1 Introduction

Drop-on-demand (DOD) inkjet printing has, over decades of development and improvements, become a popular additive manufacturing process in myriad technological applications, extending far beyond its original motivation in conventional printing and the computer graphics [1–3]. In recent years, it has also been used for fabricating flexible electronics [4], solder dispensing in flip-chip manufacturing [5], tissue engineering [6, 7], and 3D printing [8, 9], among others. Its operational success relies primarily on the controllability of ink droplet ejection when actuated by an impulse signal, commonly through the squeezing action induced by piezoelectric deformation or the expansion of a vapor bubble in the ink chamber on a heater pad, to effectively propel a desired volume of liquid ink out of the nozzle orifice at sufficient speed. The droplets must be ejected with highly consistent volume and velocity, ensuring extremely high repeatability. For example, the variations in droplet volume and speed within 2%, while trajectory straightness (flying directionality) within 10 milliradians [3].

For high-quality, low-graininess printing, a smaller individual droplet volume is desirable, e.g., droplets of less than 32 pL (diameter $< 40\,\mu$m) are needed for a 600 dpi spatial resolution. Moreover, it is necessary to have the droplet travel across a nozzle-to-substrate stand-off distance (typically less than 1 mm for high-resolution printing) in a fraction of a millisecond, which demands a droplet flight velocity of at least a few meters per second [3]. When applications demand a longer stand-off distance for printing irregular substrate surfaces, a higher flight velocity is required; therefore, active research has been focused on achieving higher-velocity droplets without compromising droplet integrity [10]. In general, efforts in ejecting smaller droplets and higher flight velocities have continued in the scientific community, through both experimentation and theoretical-computational analyses [11].

The fluid dynamics of droplet ejection in DOD inkjet printing are theoretically governed by the Navier-Stokes equations with an appropriate description of the fluid free interface motion and other boundary conditions. However, mathematically solving such a complicated partial differential system is a nontrivial challenge, even with modern computational capabilities. The most popular numerical method for computing the drop ejection problem to date appears to be the volume-of-fluid (VOF) method [12, 13], as often utilized in the DOD inkjet research literature [14–19]. In the present work, a VOF solver—interIsoFoam [20, 21]—available in the open-source package Open FOAM® (v2206) is used for conveniently constructing the computational model.

In what follows, the computational model is described with nondimensionalized governing equations with influential dimensionless parameters. In the section of results and discussion, the effects of actuation strength, ink properties, droplet size with respect to the nozzle orifice size, and ink wetting angle on the wall of the nozzle orifice are systematically investigated. Finally, the main findings are summarized in the conclusions.

2 Model description

As illustrated in figure 1, the computational model includes a straight ink channel nozzle of constant diameter D with the actuation flow inlet and nozzle exit at two channel ends. The nozzle configuration is a simplified representation of those MEMS-fabricated orifices on nozzle plates. The ink is assumed to be a Newtonian liquid here. The ink droplet is ejected into an open atmosphere. Having the nozzle axis aligned with the direction of gravity, the model is considered axisymmetric for computing efficiency.

To focus on the fundamentals with a minimum number of controlling parameters, the waveform of the actuation pulse is assumed to generate a rectangular wave of ink flow velocity at the ink channel inlet [15], such that the boundary condition at the liquid ink inlet for fluid velocity is set as $\mathbf{U} = (0, 0, U_z)$ with a uniform value of U_z

$$U_z(t) = \begin{cases} U_a\,, & \text{for} \quad 0 < t < \delta\tau \\ 0\,, & \text{for} \quad t = 0 \text{ and } t \geq \delta\tau \text{ (until next actuation pulse)} \end{cases} , \tag{1}$$

where U_a= $const$ is the actuation velocity amplitude (representing the actuation strength) and $\delta\tau$ the pulse width, as the simplest actuation waveform.

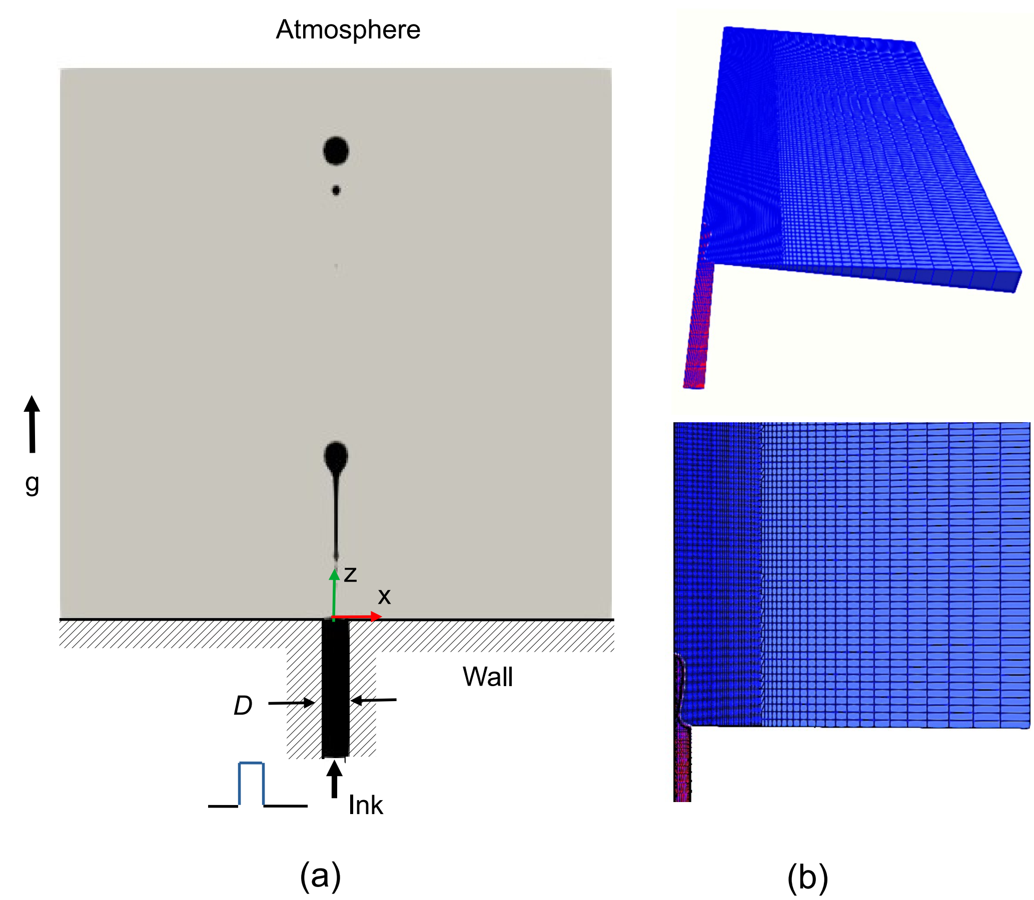

Figure 1: (a) Computational model for droplet ejection in DOD inkjet devices; (b) An illustrative wedge mesh (discretized into quadrilateral finite-volume cells in two-dimensional space) with a combination of fine and coarse patches stitched together

2.1 Governing equations

The VOF vector form of the Navier-Stokes equations in OpenFOAM® is usually written as

$$\frac{\partial(\rho\mathbf{U})}{\partial t} + \nabla\cdot(\rho\mathbf{U}\mathbf{U}) - \nabla\cdot\{\mu\left[\nabla\mathbf{U} + (\nabla\mathbf{U})^T\right]\} = -\nabla p_{rgh} + \sigma\kappa\nabla\alpha \quad , \tag{2}$$

with p denoting the piezometric pressure (having the hydrostatic pressure lumped in), σ the surface tension, and κ the mean curvature of free surface

$$p_{rgh} = p - \rho g \mathbf{e_g}\cdot\mathbf{x} \quad \text{and} \quad \kappa = \nabla\cdot\left(\frac{\nabla\alpha}{|\nabla\alpha|}\right) \quad . \tag{3}$$

Here, $\alpha(\mathbf{x},t)$ is an indicator function (also called the phase fraction function) with the VOF method, where $\alpha = 0$ is assigned in the cells containing one fluid phase (e.g., the gas phase) and $\alpha = 1$ in the cells of the other fluid phase (e.g., the liquid phase), while the cells of the fluid interface have $0 < \alpha < 1$. The transport of α is governed by the advection equation

$$\frac{\partial \alpha}{\partial t} + \nabla\cdot(\alpha \mathbf{U}) + \nabla\cdot\left[\alpha(1-\alpha)\mathbf{U_r}\right] = 0 \quad , \tag{4}$$

where $\mathbf{U_r}$ is the relative compression velocity used to prevent the interface from smearing numerically.

The VOF fluid properties are defined as time-dependent distributed field functions using $\alpha(\mathbf{x},t)$ as a weight. For example, the density and dynamic viscosity of a liquid-gas two-phase system are written as

$$\rho(\mathbf{x},t) = \alpha\rho_l + (1-\alpha)\rho_g \quad \text{and} \quad \mu(\mathbf{x},t) = \alpha\mu_l + (1-\alpha)\mu_g \quad , \tag{5}$$

Thus, the mass conservation equation, even for incompressible flow, takes the form

$$\frac{\partial \rho}{\partial t} + \nabla\cdot(\rho \mathbf{U}) = 0 \quad , \tag{6}$$

because the fluid phase interface is treated as an internal field in VOF, rather than a boundary between different phases.

2.2 Nondimensional formulations

A straightforward way to set up the nondimensional model is to measure length $\mathbf{x}$ in units of the inkjet nozzle orifice diameter D (e.g., $\tilde{z} = \mathbf{e_g}\cdot\mathbf{x}/D$ in figure 1), fluid velocity $\mathbf{U}$ in U_a, time t in D/U_a, fluid density ρ in ρ_l, dynamic viscosity μ in μ_l, thermodynamic pressure p in $\mu_l U_a/D$ (i.e., $\tilde{p} = pD/(\mu_l U_a)$), and gravitational acceleration g in U_a^2/D (i.e., $\tilde{g} = gD/U_a^2$), transforming (2) to a nondimensional form

$$Re\left[\frac{\partial(\tilde{\rho}\tilde{\mathbf{U}})}{\partial \tilde{t}} + \tilde{\nabla}\cdot(\tilde{\rho}\tilde{\mathbf{U}}\tilde{\mathbf{U}})\right] - \tilde{\nabla}\cdot\{\tilde{\mu}\left[\tilde{\nabla}\tilde{\mathbf{U}} + (\tilde{\nabla}\tilde{\mathbf{U}})^T\right]\} = -\tilde{\nabla}\left(\tilde{p} - Re\tilde{\rho}\tilde{g}\tilde{z}\right) + \frac{\tilde{\kappa}\tilde{\nabla}\alpha}{Ca} \; , \tag{7}$$

where

$$\tilde{\rho} \equiv \alpha + (1-\alpha)\rho_g/\rho_l \text{ and } \tilde{\mu} \equiv \alpha + (1-\alpha)\mu_g/\mu_l \tag{8}$$

are dimensionless fluid properties, and the Reynolds number Re and capillary number Ca,

$$Re \equiv \frac{\rho_l U_a D}{\mu_l} \text{ and } Ca \equiv \frac{\mu_l U_a}{\sigma} \quad , \tag{9}$$

are dimensionless parameters.

As a consequence, the nondimensional inlet velocity condition (1) simply becomes

$$\tilde{U}_z(\tilde{t}) = \begin{cases} 1\,, & \text{for } \ 0 < \tilde{t} < \delta\tilde{\tau} \\ 0\,, & \text{for } \ \tilde{t} = 0 \text{ and } \tilde{t} \geq \delta\tilde{\tau} \text{ (until next actuation pulse)} \end{cases} \quad , \tag{10}$$

where $\delta\tilde{\tau} = \delta\tau U_a/D$. To complete the model specification, other boundary conditions (available in the OpenFOAM® package) for $\tilde{\mathbf{U}}$ are *noslip* at solid wall and *pressureInletOutletVelocity* at the far-field boundary of open atmosphere, while those for $\tilde{p}$ are *fixed value* $\tilde{p} = 0$ at the far-field boundary and *zeroGradient* at all other boundaries.

For VOF computation, the fluid interface is described by the dimensionless phase fraction function α governed by (4), which does not introduce new parameters when nondimensionalized, as (6). This phase fraction function α requires a boundary condition specified at the gas-liquid-solid three-phase contact line, where the *dynamicAlphaContactAngle* (readily available in the OpenFOAM® package) is used in the present work by specifying the static contact angle θ_0, advancing contact angle θ_A (e.g., $= \theta_0 + 15^o$), and receding contact angle θ_R (e.g., $= \theta_0 - 15^o$). Like all macroscopic continuum models, the OpenFOAM® implementation of the dynamic contact angle code is based on an empirical formula that contains an *ad hoc* parameter, u_θ, for scaling the contact line sliding velocity on the solid wall, to enable calibrating computational results for matching specific experimental data. Here in this work, the value of dimensionless $\tilde{u}_\theta$ is set to 1, to simplify the analysis for logical consistency.

In view of the nondimensional governing equations presented here, it becomes clear that the mathematical system is controlled primarily by the dimensionless parameter values of Re,

Ca, and $\delta\tilde{\tau}$ (though appearing in (7), the value of $\tilde{g}$ is usually negligibly small in DOD inkjet applications). While Re and Ca determine the fluid dynamic behavior, the size of the ejected droplet is controlled by $\delta\tilde{\tau}$. In the DOD inkjet research literature, however, the most commonly mentioned dimensionless parameters are the Reynolds number Re and Weber number We ($=$ $Re\,Ca$); some authors believe the most important parameter is

$$Z = \sqrt{\frac{Re}{Ca}} \equiv \frac{\sqrt{\rho_l D \sigma}}{\mu_l} \quad \left(= \frac{1}{Oh}\right) \tag{11}$$

(where Oh denotes the Ohnesorge number [11]) for droplet ejection [16–19] following the suggestion of Fromm [22]. It should be noted that among Re, Ca, We, and Z, there can only be two independent parameters. Moreover, the contact angle θ_0 at the three-phase contact line can play an important role [18], as also shown with the bubble formation problem [23–25]. Thus, the present work would focus on examining the effects of independent parameters Re, Z, $\delta\tilde{\tau}$, and θ_0, for gaining insights into basic phenomena to enhance our fundamental understanding. Here, the values of Ca ($= Re/Z^2$) and We ($= Re^2/Z^2$) can simply be calculated from the given Re and Z.

2.3 Dimensionless parameter input

In general, the input parameters in OpenFOAM® are typically as their physical values in SI units, i.e., 1.2 (kg m^{-3}) for ρ_g of ambient air, 0.07 (kg s^{-2}) for σ of the air-water interface, etc. To properly input dimensionless parameters in the *interIsoFoam* case dictionary, a self-consistent way for parameter value conversion is needed. Table 1 provides the list of those input dimensionless parameters in place of the corresponding dimensional physical parameters in the *interIsoFoam* case dictionaries, for convenient reference.

According to table 1, the dimensionless value of $\mu_l = \nu_l \rho_l$ becomes a constant 1, and that of μ_g/μ_l in (8) can be determined from the given $(\nu_g \rho_g)/(\nu_l \rho_l)$. With U_a in the boundary

Table 1: Present model input dimensionless parameters for those corresponding physical ones in the *interIsoFoam* case dictionaries

Original	Dimensionless Input
ρ_g (kg m^{-3})	ρ_g/ρ_l
ν_g (m^2 s^{-1})	ν_g/ν_l
ρ_l (kg m^{-3})	Re
ν_l (m^2 s^{-1})	$1/Re$
σ (N m^{-1})	Z^2/Re (= $1/Ca$)
g (m s^{-2})	$\tilde{g} = gD/(U_a^2)$
U_a (m s^{-1})	1
$\delta\tau$ (s)	$\delta\tilde{\tau} = \delta\tau U_a/D$

condition dictionary becoming a constant 1, the eight original dimensional parameters to be specified are reduced to six dimensionless ones, namely ρ_g/ρ_l, ν_g/ν_l, Re, Z, $\tilde{g}$, and $\delta\tilde{\tau}$.

3 Results and discussion

By considering the fact that most available high-resolution DOD inkjet printers use nozzle orifices with D from 20 to 50 μm and liquid inks usually with $\rho_l = 1000 \pm 10\%$ kg m^{-3}, $1 \leq \mu_l \leq 20$ cp and $0.02 \leq \sigma \leq 0.07$ N m^{-1}, it seems reasonable to start with considering $D = 2.5 \times 10^{-5}$ (for producing $\sim$ 10 pL droplets), $\rho_l = 1000$, $\mu_l = 0.01$ (= 10 cp), and $\sigma = 0.04$ for estimating reference values of Z (= 3.1623) and Re (= 25) with $U_a = 10$ m s^{-1}. Assuming the gas phase is the ambient air with $\rho_g = 1.2$ kg m^{-3} and $\mu_g = 1.8 \times 10^{-5}$ kg m^{-1} s^{-1}, the values of ρ_g/ρ_l and μ_g/μ_l become 1.2×10^{-3} and 1.8×10^{-3} (leading to $\nu_g/\nu_l = 1.5$), respectively. Moreover, the value of $\tilde{g}$ now becomes 2.45×10^{-6}, indicating that the hydrostatic pressure effect is inconsequential in (7) and practically negligible in inkjet printing (which also corroborates with the fact that the terminal velocity of a droplet with $d \sim 25$ μm in the earth-bound gravitational field is $\rho_l g d^2/(18\mu_g) \sim 0.019$ m s^{-1}, less than one percent of typical inkjet droplet flight velocity.)

To produce < 10 pL droplets corresponding to diameters $d < 26.7$ μm with a nozzle of $D = 25$ μm and $U_a = 10$ (m s^{-1}), the value of $\delta\tau$ should be < 2.037 μs, which yields $\delta\tilde{\tau} < 0.8149$. With the nondimensional $\delta\tilde{\tau} = 0.8149$ and $\tilde{U}_a = 1$, the nondimensional volume of ink pushed out of the nozzle is $\pi\delta\tilde{\tau}/4 = 0.64$, corresponding to the nondimensional droplet diameter $\tilde{d} = d/D = 1.069$ (or $d = 26.73$ μm). If $\delta\tilde{\tau}$ is set as 0.6667 ($= 2/3$), the value of $\tilde{d}$ becomes 1 (corresponding to the 8.18 pL droplets of $d = 25$ μm with a $D = 25$ μm nozzle.)

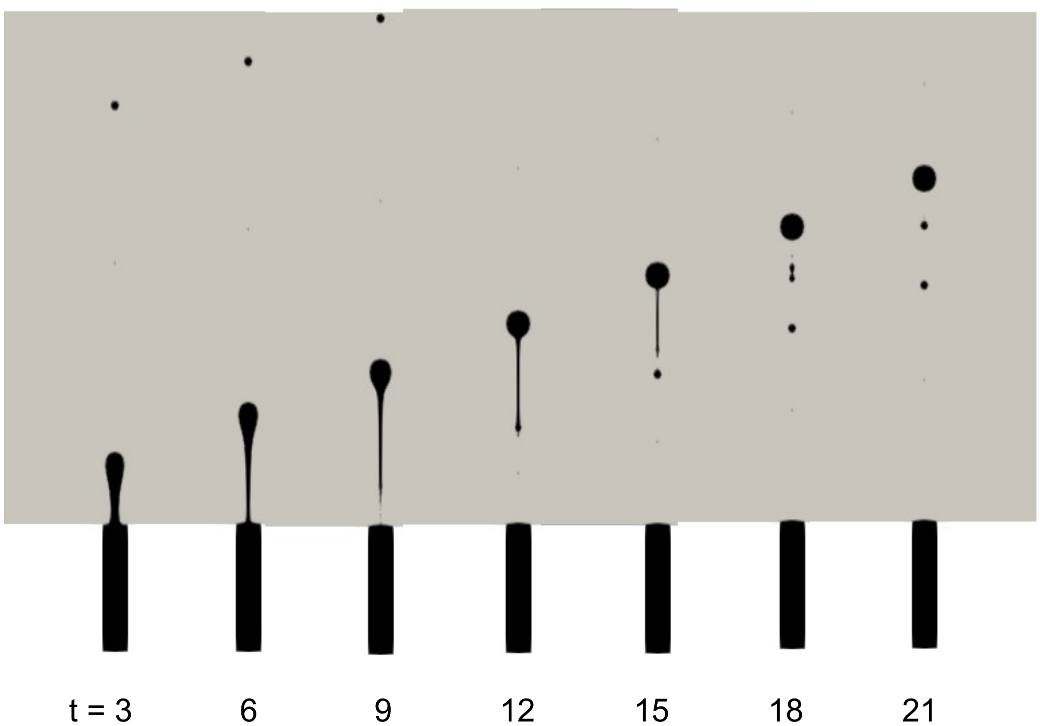

Figure 2: Images of computed droplet ejection results at $\tilde{t} = 3, 6, 9..., 21$ (from the initiation of actuation) for the case of $Re = 25$, $Z = 3.1623$, $\nu_g/\nu_l = 1.5$, and $\delta\tilde{\tau} = 0.6667$ (for generating droplets of $\tilde{d} = 1$), with $\theta_0 = 60^o$ ($\theta_A = 75^o$ and $\theta_R = 45^o$)

Figure 2 displays a series of images of computed droplet ejection results at nondimensional time $\tilde{t} = 3, 6, 9, ..., 21$ for $Re = 25$, $Z = 3.1623$, and $\delta\tilde{\tau} = 0.6667$ with $\theta_0 = 60^o$. Here, the shape evolution of the meniscus and ejected droplet looks quite similar to visualization images often seen in the literature [10, 14, 17, 26]. In response to the actuation pulse, the front of the ink meniscus is stretched forward, moving out of the nozzle orifice, with the formation of a narrowing neck that finally pinches off to form an ejected droplet, which takes place in a much longer timescale (e.g., at $\tilde{t} \sim 8$) than the actuation pulse width $\delta\tilde{\tau}$ $(= 0.6667)$. The radial contracting long tail behind the round droplet head tends to break up into smaller satellites, which are usually undesirable for inkjet printing [11].

3.1 Effect of Re—actuation strength

Since the value of Z is determined only by the nozzle size and ink properties, keeping the value of Z fixed while varying Re represents the situation of adjusting the actuation strength U_a for a given nozzle with a given ink. With the nondimensional variables, $\delta\tilde{\tau} = 0.6667$ means the ejected droplet size $\tilde{d} = 1$, the same as the nozzle orifice diameter.

The dynamic behavior of the droplet ejection process shown in figure 3 reveals that the moving speed of the meniscus front at $\tilde{t} \sim 1$ is $\tilde{U}_z \sim 1$, about the same as U_a when converted to its physical dimensions (almost independent of the value of Re). The frontal moving speed of the meniscus and ejected droplet decreases with the reduction of Re as soon as $\tilde{t} > 2$, and the droplet's flight velocity continuously decreases with time and distance, due to the air drag force.

A relatively larger Re tends to elongate the thin tail behind the ejected droplet head (e.g., those with $Re > 20$ in figures 2 and 3), while the long tail may disappear when Re is reduced below a threshold value (e.g., for $Re < 20$ in figure 3). Because those long droplet tails often produce unwanted satellites that could lead to generally detrimental effects to print quality and nozzle clogging, the subject of fluid filament breakup dynamics has been intensively studied over decades by many authors [27–31] due to its relevance to the inkjet droplet ejection process, pinch-off, and satellite formation [11].

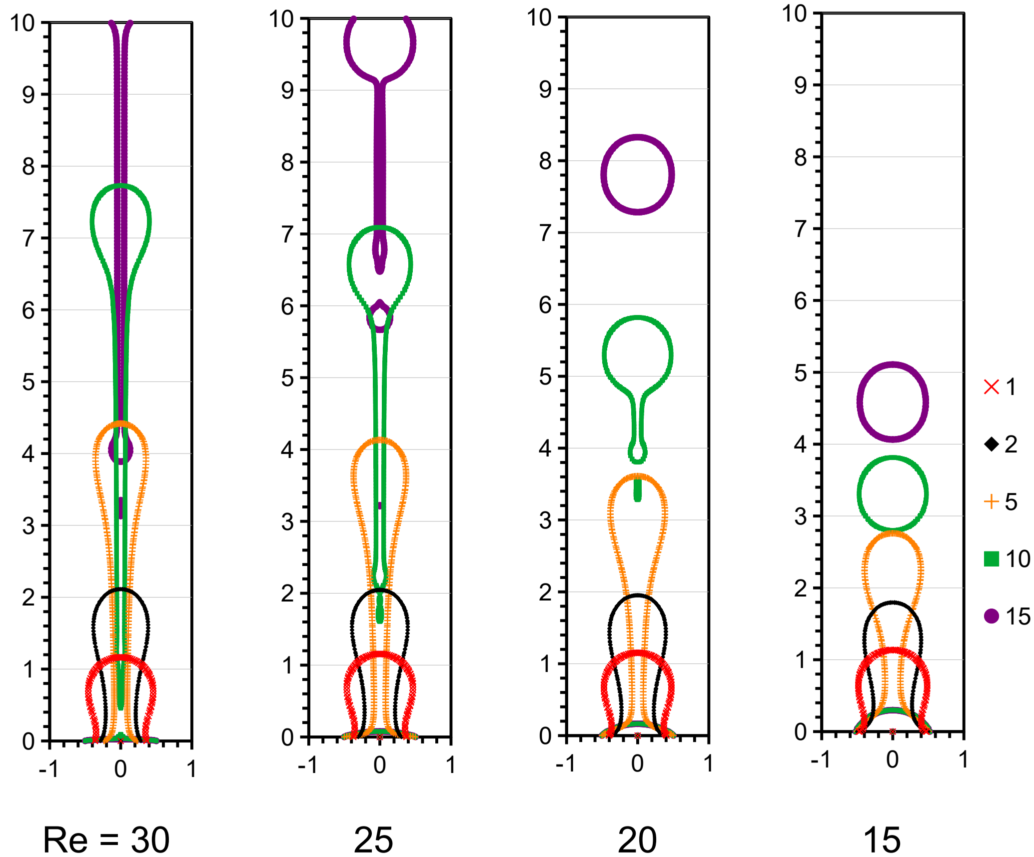

Figure 3: Droplets ejected at $Re = 30, 25, 20, 15$ (for $U_a = 12, 10, 8, 6$ m s^{-1}) while maintaining $Z = 3.1623$, $\nu_g/\nu_l = 1.5$, $\delta\tilde{\tau} = 0.6667$, and $\theta_0 = 60^o$ at $\tilde{t} = 1, 2, 5, 10, 15$

If the ink in the case of figure 3 is changed to an aqueous ink with very dilute functional material loading, the value of Z becomes 41.833 (corresponding to $\mu_l = 1$ cp and $\sigma = 0.07$ N/m), $\nu_g/\nu_l = 15$, and $Re = 25 \times U_a$. Figure 4 shows that with $Z = 41.833$, the threshold value of Re for satellite-generating long droplet tail formation seems to be ~ 300. Thus, the threshold value of Re for satellite formation can obviously depend on the value of Z. Many authors summarized the operational window of DOD inkjet in plots of Z (or Oh) versus Re [11, 32]. Interestingly, when the value of Re/Z ($\sqrt{We}$) is examined, it becomes clear that $20/3.1623 =$

6.33246 is not too far from $300/41.833 = 7.1714$, suggesting that satellite formation be mainly controlled by the value of Re/Z ($= \sqrt{We}$) (apparently, $Re/Z < 7$ for a large range of Z could prevent satellite generation, which seems also consistent with some of the experiments [e.g., 33]) rather than that of Re, as suggested by some authors to present a Z-We diagram for illustrating the DOD inkjet operational window [34].

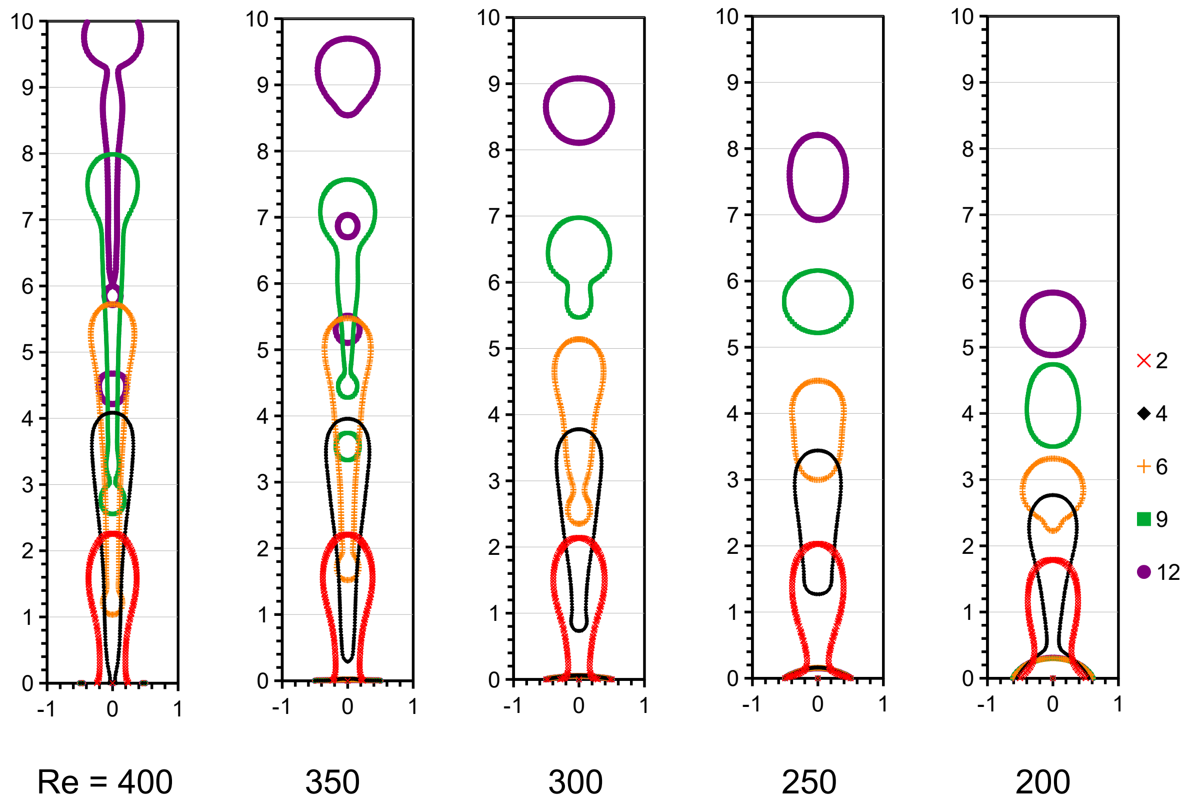

Figure 4: As figure 3 but at $Re = 400, 350, 300, 250, 200$ (for $U_a = 16, 12, 10, 8$ m s^{-1}) with fixed $Z = 41.833$ at $\tilde{t} = 2, 4, 6, 9, 12$

In terms of physical meaning,

$$\frac{Re}{Z} = U_a\sqrt{\frac{\rho_l D}{\sigma}} = \frac{U_a}{U_\sigma}\ , \text{with } U_\sigma = \sqrt{\frac{\sigma}{\rho_l D}}\quad , \tag{12}$$

is actually a nondimensional actuation strength with U_a measured in units of the capillary velocity U_σ (defined with D as the characteristic length and the timescale of capillary-driven fluid motion $\sqrt{\rho_l D^3/\sigma}$), as considered in some of the previous publications [15, 32]. Therefore, the nondimensional actuation strength Re/Z will also be used in the following discussion.

3.1.1 Momentum loss during droplet ejection

It is noticeable that the velocities of those ejected droplets in figures 3 and 4 can be substantially lower than the actuation velocity amplitude U_a, or less than 1 in terms of nondimensional droplet velocity $\tilde{U}_d$ (right after detachment from the nozzle orifice meniscus). This might be expected as a consequence of the consumption part of the input momentum $\pi\rho_l D^2 U_a^2 \delta\tau/4$ in overcoming the surface tension resistance and viscous dissipation for successful droplet ejection. Thus, a simple momentum budget equation becomes

$$\frac{\pi\rho_l D^2 U_a^2 \delta\tau}{4} = \frac{\pi\rho_l D^2 U_a \delta\tau}{4} U_d + \lambda \text{ , or } \tilde{\lambda} = 1 - \tilde{U}_d \quad , \tag{13}$$

where $\tilde{\lambda} = 4\lambda/(\pi\rho_l D^2 U_a^2 \delta\tau)$ denotes the loss fraction of the input momentum in (13), with nondimensional $\tilde{U}_d = U_d/U_a$.

Figure 5 shows a plot of $\tilde{\lambda}$ versus Re/Z for inks of $Z = 3.1623$ and 41.833, indicating inks of lower viscosities are subjected to relatively less momentum loss during the droplet ejection process at a given Re/Z (or $\sqrt{We}$). For a given ink, a stronger actuation (corresponding to higher U_a and larger Re) leads to relatively less momentum loss fraction $\tilde{\lambda}$. In view of the fact that $\tilde{\lambda} \propto 1/U_a$ for a fixed droplet volume, the value of $\tilde{\lambda} \times (Re/Z)$ turns out to be nearly constant for various of Re/Z, e.g., $\tilde{\lambda} \times (Re/Z) \sim 3.2$ and 2.3 for $Z = 3.1623$ and 41.833, respectively. This suggests that the momentum loss for a given ink and a droplet volume is nearly independent of the actuation strength, as expected based on physical intuition that such a loss should mostly be caused by the ink properties (in a certain range of the actuation strength), e.g., relatively less momentum loss for a lower viscosity ink of a greater Z value. Thus, a larger

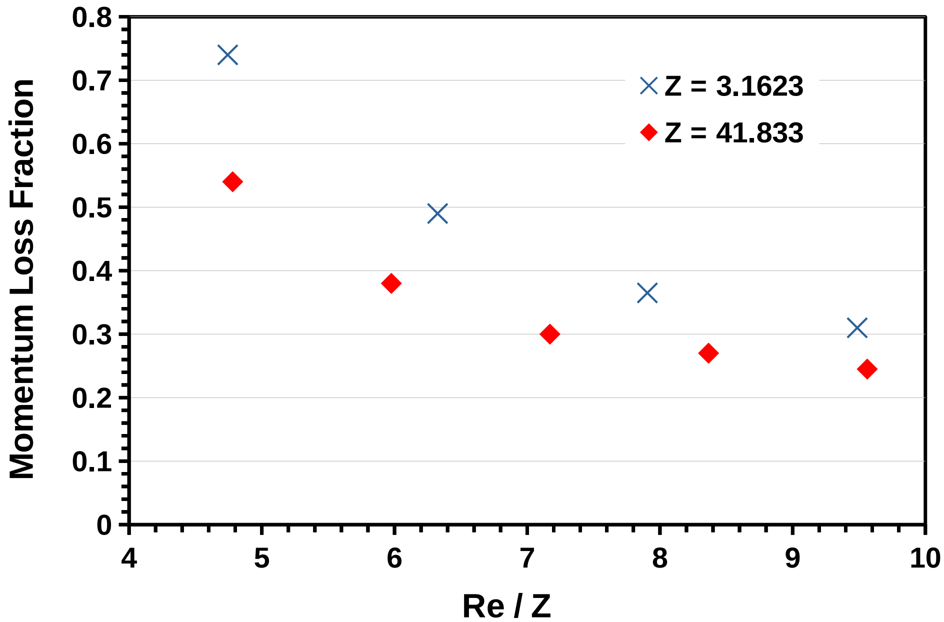

Figure 5: Loss fraction of ejected droplet momentum $\tilde{\lambda}$ versus Re/Z at $Z = 3.1623$ and 41.833 (for caes in figures 3 and 4)

fraction of input momentum can be transferred to the ejected droplet for higher flight velocity with a stronger actuation, as suggested in figure 5.

When the actuation strength is inadequate (as the value of Re/Z becomes too low), the ejected droplet cannot acquire sufficient momentum for DOD inkjet printing because of the lack of needed flight velocity. For example, the cases with $U_a = 8$ m s^{-1}, corresponding to $Re = 20$ in figure 3 and 200 in figure 4 ($Re/Z \sim 6.32$ and 4.78 in figure 5 at $Z = 3.1623$ and 41.833) would have $\tilde{U}_d \sim 0.5$ or a droplet flight velocity $U_d \sim 4$ m s^{-1}. Thus, an actuation strength $U_a < 8$ m s^{-1} might not be adequate for DOD inkjet printing for droplets of $d/D \sim 1$.

3.1.2 Velocity decline of ejected droplet due to air drag

If the ejected droplet is simplified to a spherical particle (by ignoring the free surface deformations, etc.), the equation governing the rectilinear flight velocity of an ink droplet $\tilde{U}_p(\tilde{t})$ can be written as [35–37]

$$\frac{d\tilde{U}_p}{d\tilde{t}} = -\frac{18\,\rho_g}{Re_p\,\rho_p}\left(1+\frac{Re_p^{2/3}}{6}\tilde{U}_p^{2/3}\right)\tilde{U}_p \text{ , with } Re_p \equiv \frac{d_p\,U_d(0)}{\nu_g} \tag{14}$$

denoting the "particle Reynolds number", where d_p is the particle diameter, $\tilde{t} = tU_p(0)/d_p$ and $\tilde{U}_p = U_p/U_p(0)$. It turns out that (14) can be rearranged as

$$\frac{d\left(\tilde{U_p}^{-2/3}\right)}{d\tilde{t}} = \frac{12\,\rho_g}{Re_p\,\rho_p}\left(\tilde{U_p}^{-2/3}+\frac{Re_p^{2/3}}{6}\right) \quad ,$$

which yields an analytical solution to (14) for $\tilde{U}_p(0) = 1$, same as that obtained by Serafini [36],

$$\tilde{U}_p(\tilde{t}) = \left[\left(1+\frac{Re_p^{2/3}}{6}\right)\exp\left(\frac{12\,\rho_g}{Re_p\,\rho_p}\tilde{t}\right)-\frac{Re_p^{2/3}}{6}\right]^{-3/2} = \frac{6\sqrt{6}}{Re_p\,\Phi(\tilde{t})^3}\ , \tag{15}$$

with

$$\Phi(\tilde{t}) \equiv \sqrt{\left(\frac{6+Re_p^{2/3}}{Re_p^{2/3}}\right)\exp\left(\frac{12\,\rho_g}{Re_p\,\rho_p}\tilde{t}\right)-1} \quad .$$

The particle flight distance as a function of flight time can also be derived by integrating $\tilde{U}_p(\tilde{t})$ given by (15) from 0 to $\tilde{t}$ as

$$\tilde{z}(\tilde{t}) = \sqrt{6}\frac{\rho_p}{\rho_g}\left\{\frac{1}{\Phi(0)}-\frac{1}{\Phi(\tilde{t})}+\tan^{-1}[\Phi(0)]-\tan^{-1}[\Phi(\tilde{t})]\right\} \quad . \tag{16}$$

Then, the stop distance (or the maximum achievable flight distance) of an ejected droplet becomes [36, 37]

$$\tilde{z}(\infty) = \sqrt{6}\frac{\rho_p}{\rho_g}\left[\sqrt{\frac{Re_p^{2/3}}{6}}+\tan^{-1}\left(\sqrt{\frac{6}{Re_p^{2/3}}}\right)-\frac{\pi}{2}\right] \text{ , because } \Phi(0) = \sqrt{\frac{6}{Re_p^{2/3}}} \quad . \tag{17}$$

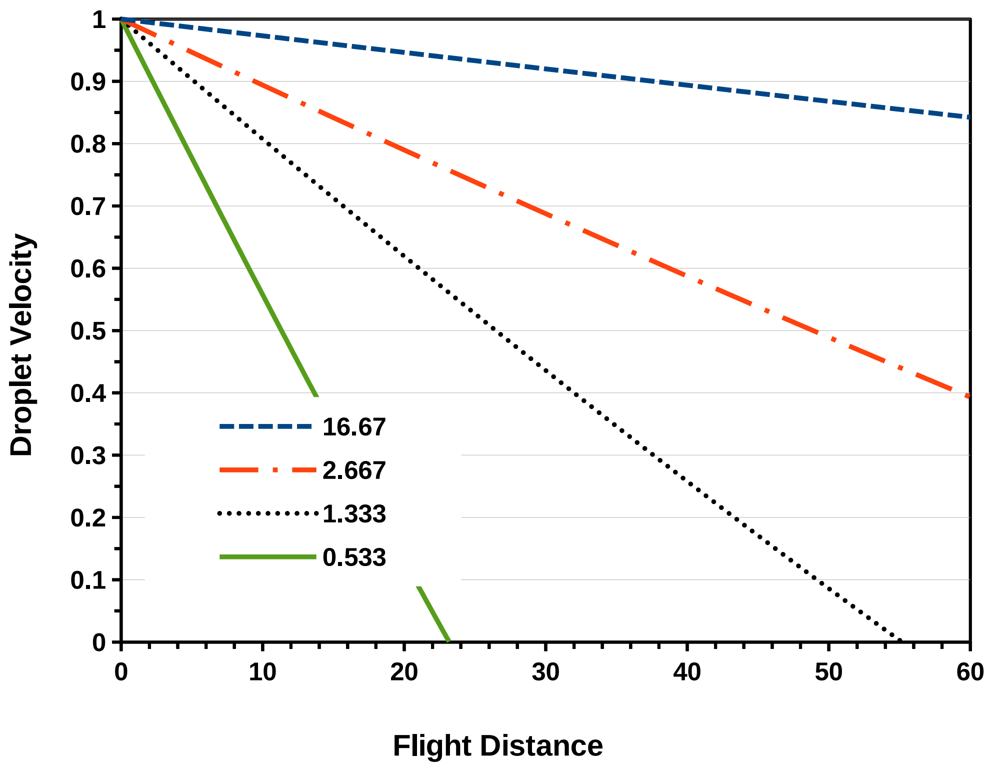

Figure 6: Droplet velocity $\tilde{U}_p$ as a function of flight distance $\tilde{z}$ for $Re_p = 16.67$, 2.667, 1.333, and 0.533

Relevant to investigations of certain inkjet printing defects [38], figure 6 shows several representative curves of $\tilde{U}_p$ versus $\tilde{z}$ according to (15) and (16). It is clear that the flight velocities of typical DOD inkjet droplets about $d \sim 25$ (μm) with $U_p(0) \sim 10$ (m s^{-1}) are not influenced significantly by ambient air drag, e.g., U_p at $z = 1$ mm becomes $\sim 0.9 \times U_p(0)$, correspondong to $\tilde{z} = 40$ when $\tilde{t} \sim 41.4$ as determined with (16), having a stop distance of $482.67 \times 0.025 \sim 12$ mm (cf. table 2). However, a droplet of $d \sim 20$ μm with a relatively lower initial velocity of $U_p(0) \sim 2$ (m s^{-1}) would take $\tilde{t} \sim 68.4$ to reach $\tilde{z} \sim 50$ or $z \sim 1$ mm, where the value of $\tilde{U}_p \sim 0.5$ (reducing to one half that of the initial value), with a stop distance of $104.08 \times 0.02 \sim 2.1$ mm. For those small satellites (e.g., with $d_p = 5$ and 2 μm with an initial velocity of 4 m s^{-1}, having stop distances of $55.184 \times 0.005 \sim 0.28$ and $23.185 \times 0.002 \sim 0.046$

Table 2: Values of Re_p in (14) for representative droplet parameters relevant to DOD inkjet printing (with ρ_g/ρ_p assumed to be 0.0012 and $\nu_g = 1.5 \times 10^{-5}$ m^2 s^{-1})

Re_p	d_p (μm)	$U_p(0)$ (m / s)	$\Phi(0)$	$\tilde{z}(\infty)$	Circumstance
16.67	25	10	0.9589	482.67	typical inkjet droplet
2.667	20	2	1.7664	104.08	slow inkjet droplet
1.333	5	4	2.2256	55.184	large satellite
0.533	2	4	3.0205	23.185	small satellite

mm in table 2), however, their flight velocities would be reduced to 0 before reaching a stand-off distance between the nozzle and substrate of $z = 1$ mm.

The quantitative estimate of the air drag effect on the droplet flight velocity also reveals a challenge to increasing the stand-off distance between nozzle and substrate, which effectively increases the needed flight time for more severe velocity decline, worse for slower droplets, in DOD inkjet printing. To compensate for such a challenge, stronger actuation with a higher U_a would be required. But a higher U_a (leading to larger Re for a given ink) tends to generate droplets with longer tails and more undesirable satellites, as shown in figures 3 and 4. This is why efforts have been continuously made in generating droplets with high flight velocities (while maintaining good droplet quality) in DOD inkjet printing research [10, 26, 39].

3.2 Effect of Z—ink properties

As mentioned above, a change of the Z value for a given nozzle size corresponds to a change of ink properties. Figure 7 shows the effect of varying Z (by varying the ink surface tension) at two different values of Re (corresponding to inks with a low viscosity and a high viscosity), as detailed in table 3. Based on the momentum loss estimates (13) suggesting $U_a \geq 8$ m s^{-1} for generating droplets of $d/D \sim 1$ with adequate flight velocity, $U_a = 8$ and 10 are considered here in Fig. 7 and Table 3 (for $D = 25$ μm and $d/D = 1$ with $\Delta\tilde{\tau} = 2/3$).

Again, the threshold value Re/Z for satellite formation seems to be around 7, i.e., multiple

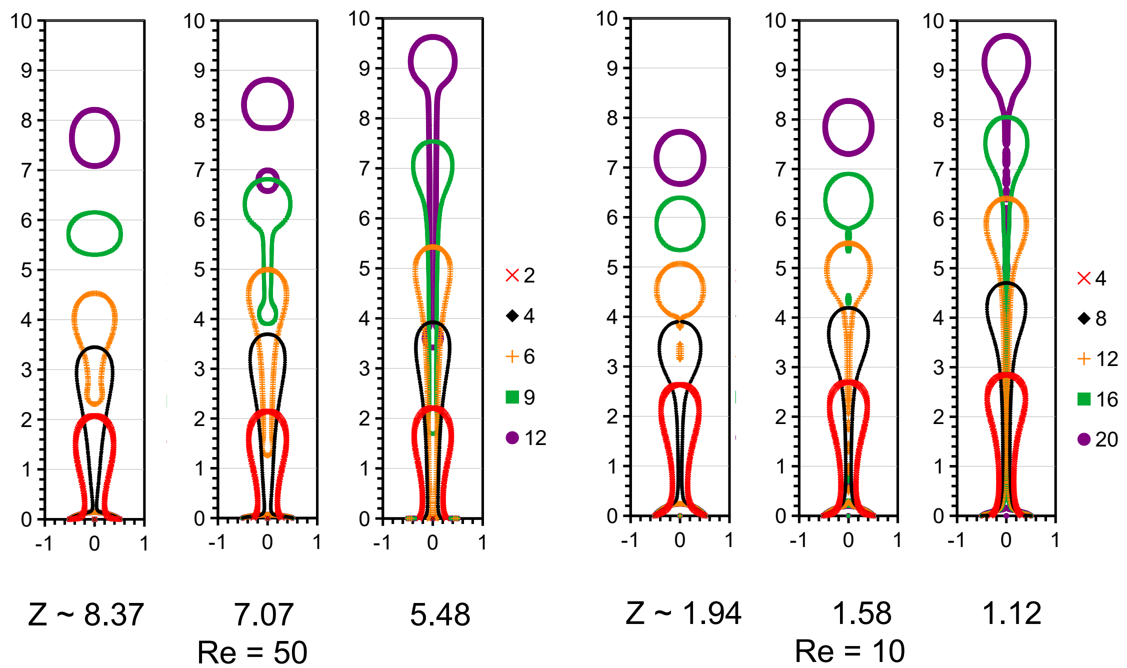

Figure 7: As figure 3 but for $Z \sim 8.37, 7.07, 5.48$ with fixed $Re = 50$ (corresponding to $Re/Z \sim 5.98, 7.07, 9.13$) at $\tilde{t} = 2, 4, 6, 9, 12$, and $Z \sim 1.94, 1.58, 1.12$ with fixed $Re = 10$ (corresponding to $Re/Z \sim 5.16, 6.33, 8.94$) at $\tilde{t} = 4, 8, 12, 16, 20$

satellites would certainly appear after formation of a long droplet tail when $Re/Z >> 7$. For the cases of $Re/Z \sim 7$, the ejected droplet tail appears either short, producing one or two transient satellites that would later coalesce with the main droplet (as shown in figure 7 for $Z = 7.07$ at $Re = 50$), or tiny, leading to miniature satellites that then quickly rejoin the main droplet (as shown in figure 7 for $Z > 1.5$ at $Re = 10$).

Because a relatively larger Z value corresponds to greater surface tension in figure 7, inks with increased surface tension, though desired for producing better quality droplets with fewer satellites, appear to cause more momentum loss of ejected droplets (which could be compensated by using stronger actuation; but too great a value of U_a tends to form long tails detrimental

Table 3: Actuation strength, ink properties (in SI units), and corresponding input dimensionless parameter values for cases in figure 7 at various Z at $Re = 50$ and 10, with $D = 25$ μm, $\delta\tilde{\tau} = 0.6667$, $\rho_g/\rho_l = 1.2 \times 10^{-3}$, and $\theta_0 = 60^o$

U_a	μ_l	σ	Re	Z	$1/Ca$	ν_g/ν_l	Re/Z	$\tilde{U}_d$	Droplet Quality
10	0.005	0.07	50	8.367	1.4	3.00	5.976	0.66	single droplet
10	0.005	0.05	50	7.071	1.0	3.00	7.071	0.68	one transient satellite
10	0.005	0.03	50	5.477	0.6	3.00	9.129	0.72	long tail, multiple satellites
8	0.02	0.06	10	1.937	0.735	0.75	5.164	0.33	tiny tail, single droplet
8	0.02	0.04	10	1.581	0.250	0.75	6.325	0.37	short tail, single droplet
8	0.02	0.02	10	1.118	0.125	0.75	8.944	0.42	long tail, multiple satellites

to the droplet quality). Of course, such a momentum loss is also intensified with inks of higher viscosity (as indicated by the values of $\tilde{U}_d = 1 - \tilde{\lambda}$ in table 3), which also tends to produce longer undesired droplet tails and more satellites. Thus, inks with higher viscosities are generally more challenging for generating high-quality droplets, while higher ink surface tension often seems desirable (although droplet velocity could be compromised somewhat).

The complex effects of various dimensionless parameters on DOD inkjet printing have been discussed by numerous authors in the literature [e.g., 2, 3, 11], but attention has rarely been paid to the effects of droplet size with respect to the nozzle size, d/D. It has been a common practice in inkjet printing to use smaller nozzle orifices for producing smaller droplets, while recognizing the fact that smaller nozzle orifices are more vulnerable to clogging, which frustrates an attempt to sustain droplet ejection reliability.

3.3 Effect of $\delta\tilde{\tau}$—droplet size d/D

The cases examined so far have been restricted to the droplets of $d/D = 1$, i.e., with sizes equal to that of the nozzle orifice (by setting $\delta\tilde{\tau} = 0.6667$); now the possibility of using a given nozzle for generating droplets of sizes other than that of the nozzle, especially those droplets of diameters smaller than D is to be investigated.

With the present nondimensional model, there is only one parameter, $\delta\tilde{\tau}$, needed to determine the droplet size $\tilde{d} = d/D$ for any given D, e.g., $\delta\tilde{\tau} = 0.2$, 0.3333, 0.6667, 1.2 for $\tilde{d} \sim 0.7$, 0.8, 1, 1.2, respectively (in contrast to the dimensional counterpart that requires specifying both U_a and $\delta\tau$ even with a given D). For nozzles of $D = 25$ μm, $\delta\tilde{\tau}= 0.6667$ yields a droplet volume of 8.18 pL, and reducing $\delta\tilde{\tau}$ to $= 0.3333$ leads to 4.09 pL droplets (of $d \sim 19.84$ μm). Figure 8 shows a few images of the droplet ejection process with $\delta\tilde{\tau}= 0.3333$ at various values of Re/Z ($= \sqrt{We}$), computed using the parameter values provided in table 4.

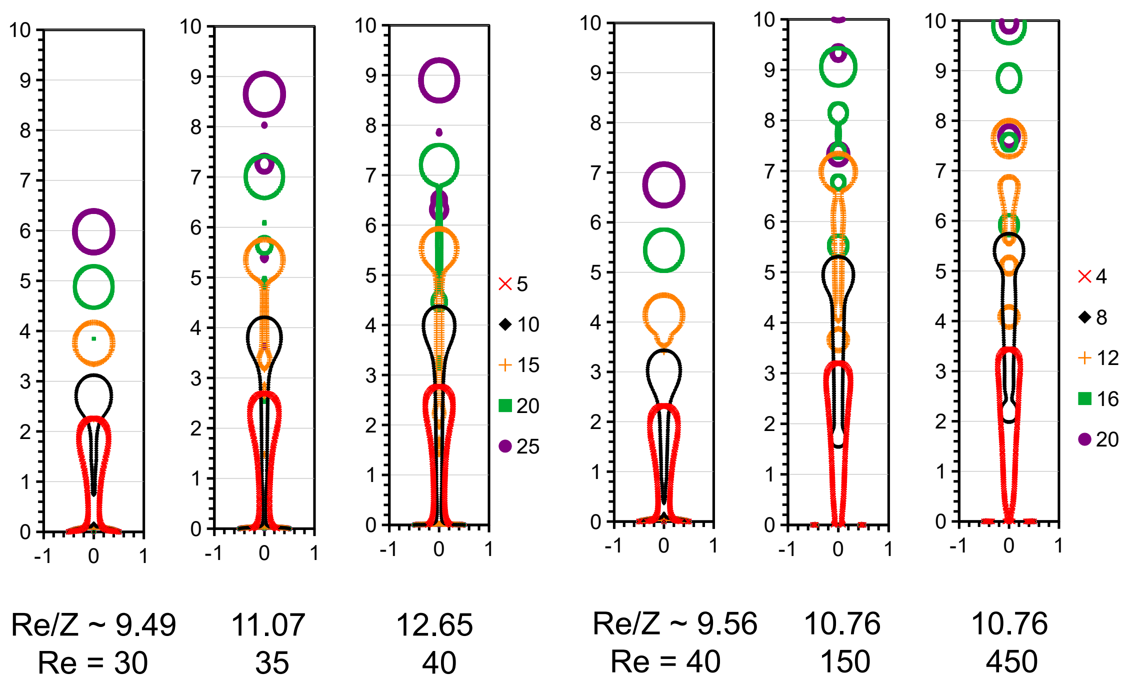

Figure 8: As figure 3 but for $Re/Z \sim 9.49$, 11.1, 12.7, 9.56, 10.76, 10.76 (with $Re = 30$, 35, 40, 40, 150, 450)

For $\delta\tilde{\tau}= 0.3333$, the threshold value of Re/Z for satellite formation seems to be around 10, unlike that ($Re/Z \sim 7$) with $\delta\tilde{\tau} = 0.6667$. Thus, the operational windows for DOD inkjet

Table 4: As table 3, but for cases in figure 8 with $\delta\tilde{\tau} = 0.3333$

U_a	μ_l	σ	Re	Z	$1/Ca$	ν_g/ν_l	Re/Z	$\tilde{U}_d$	Droplet Quality
12	0.01	0.04	30	3.162	0.333	1.5	9.487	0.22	single droplet
14	0.01	0.04	35	3.162	0.286	1.5	11.07	0.33	short tail, single satellite
16	0.01	0.04	40	3.162	0.250	1.5	12.65	0.34	long tail, multiple satellites
16	0.01	0.07	40	4.183	0.500	1.5	9.562	0.33	single droplet
18	0.003	0.07	150	13.94	1.296	5.0	10.76	0.52	one remaining satellite
18	0.001	0.07	450	41.83	3.889	15.0	10.76	0.57	two remaining satellites

printing, usually presented as diagrams in terms of Re versus Oh ($= 1/Z$) or We ($= Re^2/Z^2$) versus Z in the literature [32, 34], are actually dependent upon the value of d/D.

When $Re/Z < 10$ (with $\delta\tilde{\tau}= 0.3333$), the ejected droplets would settle to a state of a single droplet with all closeby satellites, if any, coalescing to the main droplet after a transient existence. But having $Re/Z < 10$ often corresponds to relatively low droplet velocity (cf. Table 4); e.g., with $U_a = 12$ (m s^{-1}), the ejected droplet would have a flight velocity $\sim 0.22 \times 12 = 2.64$ (m s^{-1}), less than typically desired for inkjet printing. Even with $U_a = 16$ (m s^{-1}), the ejected droplet of "good quality" could achieve a reasonable initial velocity $\sim 0.33 \times 16 = 5.28$ (m s^{-1}), which is decreasing with flight time and distance as illustrated in figure 6. As discussed around figure 5 about momentum loss during the droplet ejection process, using larger values of Re/Z (corresponding to higher actuation strength U_a) generally increases $\tilde{U}_d$ ($= 1 - \tilde{\lambda}$). But increasing Re/Z tends to compromise the quality of ejected droplets, with more satellites.

Interestingly, figure 8 and table 4 also exhibit different details of droplet ejection behavior (such as droplet velocity and number of remaining satellites) for the same Re/Z value (e.g., ~ 10.76) but different values of Re and Z. Inks with lower viscosity (or larger value of Z) tend to enable ejection of droplets with relatively higher flight velocity. Thus, the only possibility to increase droplet velocity without sacrificing the droplet quality is to adjust the ink to have a larger Z value (e.g., by reducing ink viscosity μ_l) such that a larger Re value with stronger actuation can be used (while keeping the value of Re/Z low).

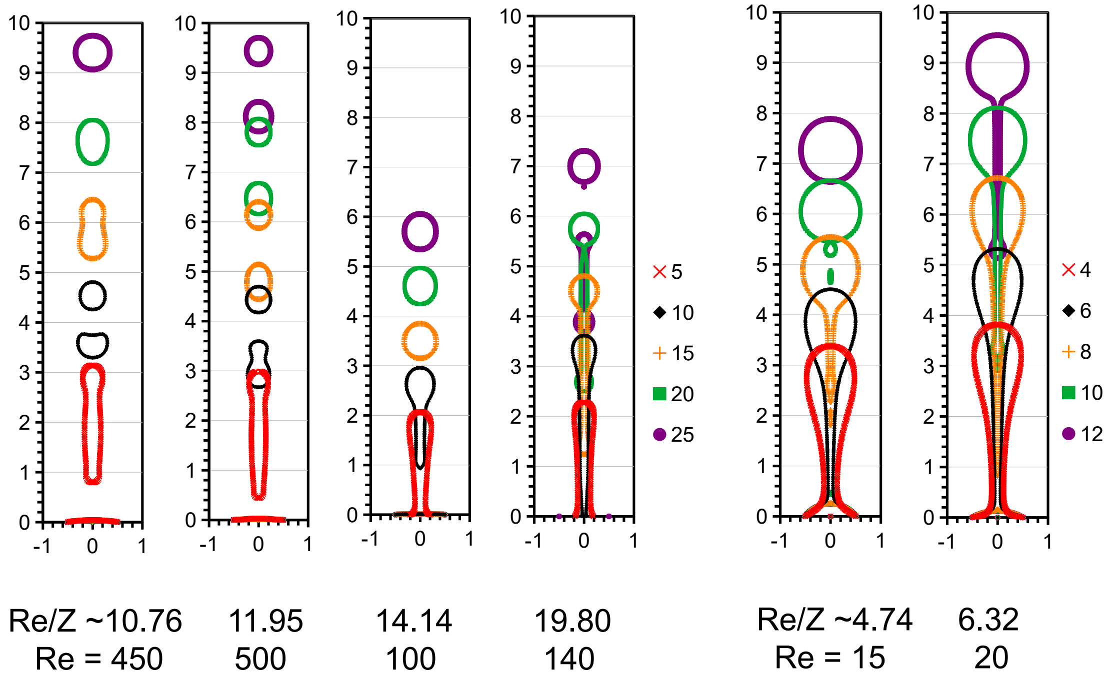

Figure 9: As figure 3 but for $Re/Z \sim 10.76, 11.95, 14.14, 19.80$ with $\delta\tilde{\tau}$ to 0.2 and $Re/Z \sim 4.74, 6.32$ with $\delta\tilde{\tau}$ to 1.2

Further reducing $\delta\tilde{\tau}$ to 0.2 leads to 2.45 pL droplets of $d \sim 16.74$ μm (with $D = 25$ μm). At $Re/Z = 10..76$ (with $U_a = 18$ m s^{-1} and $Re = 450$, as an example for inks of high surface tension and low viscosity), the droplet breaks into two pieces soon after detaching from the nozzle orifice, and then they reintegrate back to a single droplet a while later with $U_d \sim 0.32 \times 18 = 5.76$ m s^{-1} (cf. figure 9 and table 5). Thus, the threshold value of Re/Z for good quality droplets is increased by reducing $\delta\tilde{\tau}$. When Re/Z is increased to 11.95 (with $U_a = 20$ m s^{-1} and $Re = 500$), these two broken pieces of the ejected droplet could not restore to unity, apparently remaining as two separate pieces forever with comparable $U_d \sim 0.33 \times 20 = 6.6$ m

Table 5: As table 3, but for cases in figure 9 with $\delta\tilde{\tau} = 0.2$ and 1.2

U_a	μ_l	σ	Re	Z	$1/Ca$	ν_g/ν_l	Re/Z	$\tilde{U}_d$	Droplet Quality
					$\delta\tilde{\tau} = 0.2$				
18	0.001	0.07	450	41.83	3.889	1.5	10.76	0.32	restored single droplet
20	0.001	0.07	500	41.83	3.5	1.5	11.95	0.33	two droplets
20	0.005	0.05	100	7.071	0.667	3	14.14	0.22	single droplet
28	0.005	0.05	140	7.071	0.357	3	19.80	0.25	substantial tail, two large satellites
					$\delta\tilde{\tau} = 1.2$				
6	0.01	0.04	15	3.162	0.667	1.5	4.743	0.61	single droplet
8	0.01	0.04	20	3.162	0.5	1.5	6.325	0.75	one remaining satellite

s^{-1} (as also shown in figure 9).

However, for inks of moderate surface tension and viscosity with $\delta\tilde{\tau}$ to 0.2, e.g., at $Z \sim 7.071$ (for $\mu_l = 5$ cp and $\sigma = 0.05$ N m^{-1}), good quality droplets with velocity $U_d > 4.4$ m s^{-1} can be generated with $Re > 100$ (for $U_a > 20$ m s^{-1} as shown in Table 5). If the value of Re is raised to 140 (for $U_a = 28$ m s^{-1}), a substantial tail is formed behind the ejected droplet with velocity $U_d \sim 7$ m s^{-1}; such a tail eventually evolves into two trailing satellites.

Some cases of $\delta\tilde{\tau}$ to 1.2 for ejecting droplets of $d > D$ are also displayed in figure 9 and table 5. Briefly, good quality droplets of $d/D \sim 1.22$ with $\delta\tilde{\tau} = 1.2$ seem to be achievable at $Re/Z < 5$ (usually with $U_a < 8$ m s^{-1}, without formation of satellites. The case of $U_a = 6$ m s^{-1} in figure 9 and Table 5 shows an ejected droplet with a velocity of $0.61 \times 6 = 3.66$ m s^{-1}, having a relatively lower momentum loss $\tilde{\lambda} \sim 0.39$ than that in figure 5 for droplets of $d \sim D$ ejected at a similar value of Re/Z.

Noteworthy here is that compared with the case of $d/D \sim 1$, the value of $\tilde{U}_d$ is relatively lower for good-quality droplets of $d/D < 1$ that can be generated with higher U_a, while those of $d/D > 1$ would have higher $\tilde{U}_d$ but require lower U_a. The end results of actual dimensional droplet velocity $\tilde{U}_d \times U_a$ appear about the same (e.g., ~ 4 m s^{-1} or so as in Tables 4 and 5).

In view of the fact that the input momentum $0.25\pi D^3 U_a \delta\tilde{\tau} \propto U_a \delta\tilde{\tau}$ for a given D, a reduction of the pulse width $\delta\tilde{\tau}$ should accompany an increase of actuation strength U_a to maintain an adequate amount of ejected droplet momentum for DOD inkjet printing.

3.4 Effect of contact angle—ink wetting property

Among several parameters examined here, the most difficult one to model might be the dynamic three-phase contact line of ink, air, and the solid wall of the nozzle orifice, because there has not been a well-established, completely satisfactory theoretical description of such a boundary condition for macroscopic continuum models [40, 41]. The *dynamicAlphaContactAngle* condition implemented in the OpenFOAM® package is no exception but is based on an *ad hoc* formulation, not for exact prediction but just to keep the computation going without encountering mathematical singularities. Such an implementation has produced numerical results that compare reasonably with experiments in recent simulations for a similar two-phase flow problem of bubble detachment [24]; it can nonetheless provide useful qualitative predictions of general fluid-dynamics behavior to guide practical explorations. Therefore, the investigation here would not bother with the exact details, by only varying the static contact angle θ_0, with the advancing contact angle θ_A set at $\theta_0 + 15^o$ and the receding contact angle θ_R at $\theta_0 - 15^o$ (and $\tilde{u}_\theta = 1$). To keep the discussion concise, the cases investigated here are restricted to those of $d/D = 1$ (with $\delta\tilde{\tau} = 0.6667$) and $\theta_0 = 30^o$, 60^o, and 90^o.

Along with table 6, figure 10 shows that the ejected droplet velocity increases with increasing contact angle θ_0 (i.e., reducing the wettability of the nozzle orifice wall); for example, a 30^o increase of θ_0 could yield about a 10% increase in the droplet velocity. Moreover, the effect of increasing θ_0 is almost equivalent to increasing the actuation strength U_a, enhancing the droplet tail length, and inducing more satellites.

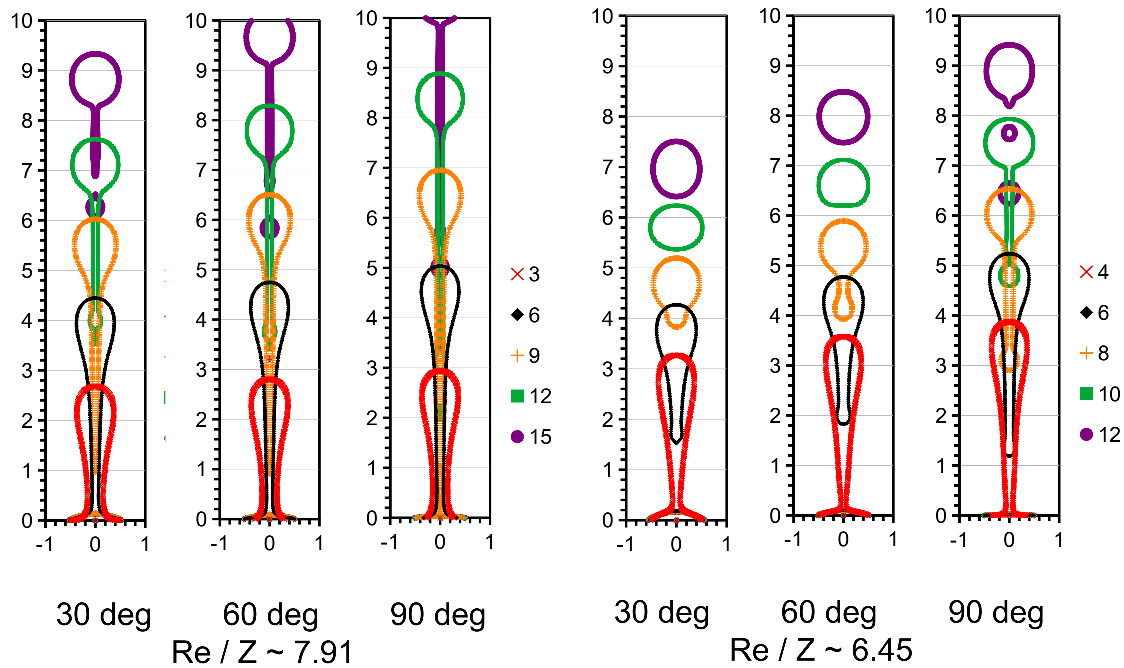

Figure 10: As figure 3 but for $\theta_0 = 30^o$, 60^o, 90^o at $Re/Z \sim 7.91$ ($Z \sim 3.16$) and 6.45 (7.75) with $\delta\tilde{\tau} = 0.6667$

4 Conclusions

The nondimensional CFD model presented here offers a clarifying description of the fundamental behavior of droplet ejection in DOD inkjet printing in terms of a few dimensionless parameters. The dimensionless parameters Re and Ca explicitly appearing in the VOF governing equations (7) can be used to construct another parameter $Z = \sqrt{Re/Ca}$ representing the ink properties, and then Re/Z serves as the nondimensional actuation strength. It is the value of Re/Z (rather than Re or Z alone) that appears to delineate the boundary that divides the desired single droplet ejected per actuation pulse and that with unwanted satellites.

The nondimensional actuation pulse width of a rectangular waveform $\delta\tilde{\tau}$ is shown to define the ejected droplet size relative to the nozzle size (e.g., d/D), which (though less discussed

Table 6: As table 3, but for cases in figure 10 with $U_a = 10$ m s^{-1}

θ_0 (deg)	μ_l	σ	Re	Z	$1/Ca$	ν_g/ν_l	Re/Z	$\tilde{U}_d$	Droplet Quality
30	0.01	0.04	25	3.162	0.4	1.5	7.91	0.58	short tail, one satellite
60	0.01	0.04	25	3.162	0.4	1.5	7.91	0.64	medium tail, two satellites
90	0.01	0.04	25	3.162	0.4	1.5	7.91	0.68	long tail, multiple satellites
30	0.005	0.06	50	7.746	1.2	3	6.45	0.6	single droplet
60	0.005	0.06	50	7.746	1.2	3	6.45	0.68	single droplet
90	0.005	0.06	50	7.746	1.2	3	6.45	0.73	one remaining satellite

by most authors) can significantly alter the parameter values in the operational windows (e.g., in a Re/Z-versus-Z diagram or similar ones) presented by many authors in the literature. Furthermore, the wetting property of an ink on the nozzle orifice wall (e.g., the ink contact angle θ_0 in the mathematical representation) is also briefly investigated to demonstrate the contact angle influence on the quality and velocity of ejected droplets.

Moreover, an analysis of momentum loss in the process of droplet ejection can provide a quantitative understanding about the actual initial velocity of a droplet after detachment from the nozzle. The time-dependent flight velocity of an ejected droplet due to air drag is shown to define the theoretical maximum nozzle-to-substate distance for a droplet with a given initial velocity.

Such a nondimensional model analysis is intended to open up a fresh perspective for investigating the keys to generating high-quality droplets with the DOD inkjet nozzles.

Funding

None

Conflict of interests

The author has no conflicts to declare

ORCID iD

James Q Feng 0000-0003-4041-3179

References

[1] G D Martin, S D Hoath, and I M Hutchings. "Inkjet printing–the physics of manipulating liquid jets and drops". *J. Phys: Conf. Series 105* (2008), p. 012001.

[2] B Derby. "Inkjet printing of functional and structural materials: fluid property requirements, feature stability, and resolution". *Ann. Rev. Mater. Res.* 40 (2010), pp. 395–414.

[3] H Wijshoff. "The dynamics of the piezo inkjet printhead operation". *Phys, Reports* 491 (2010), pp. 77–177.

[4] H Abdolmaleki, P Kidmose, and S Agarwala. "Droplet-based techniques for printing of functional inks for flexible physical sensors". *Adv. Mater.* 33.20 (2021), p. 2006792.

[5] D J Hayes, D B Wallace, and W R Cox. *MicroJet printing of solder and polymers for multi-chip modules and chip-scale packages*. Vol. 3810. Denver, CO, 1999, pp. 242–247.

[6] M Nakamura, A Kobayashi, F Takagi, A Watanabe, Y Hiruma, K Ohuchi, Y Iwasaki, M Horie, I Morita, and S Takatani. "Biocompatible inkjet printing technique for designed seeding of individual living cells". *Tissue Eng.* 11.11-12 (2005), pp. 1658–1666.

[7] J A Park, Y Lee, and S Jung. "Inkjet-based bioprinting for tissue engineering". *Organoid* 3 (2023), e12.

[8] F Sachs, M Cima, P Williams, and D Brancazio. "3-dimensional printing: rapid tooling and prototypes directly from a CAD model". *J. Eng. Ind. Trans. ASME* 114 (1992), pp. 481–488.

[9] D K Lee, K S Sin, C Shin, J-H Kim, K-T Hwang, U-S Kim, S Nahm, and K-S Han. "Fabrication of 3D structure with heterogeneous compositions using inkjet printing process". *Materialstoday Communications* 35 (2023), p. 105753.

[10] Z Yang, H Tian, C Wang, X Li, X Chen, X Chen, and J Shao. "Piezoelectric drop-on-demand inkjet printing with ultra-high droplet velocity". *Research* 6 (2023), p. 0248.

[11] D Lohse. "Funamental fluid dynamics challenges in inkjet printing". *Ann. Rev. Fluid Mech.* 54 (2022), pp. 349–382.

[12] C W Hirt and B D Nichols. "Volume of fluid (VOF) method for dynamics of free boundaries". *J. Comput. Phys.* 39 (1981), pp. 201–225.

[13] J U Brackbill, D B Kothe, and C Zemach. "A continuum method for modeling surface tension". *J. Comput. Phys.* 100 (1992), pp. 335–254.

[14] N Reis and B Derby. *Ink jet deposition of ceramic suspensions: modeling and experiments of droplet formation*. Vol. 624. 2000, pp. 65–70.

[15] J Q Feng. "A general fluid dynamic analysis of drop ejection in drop-on-demand ink jet devices". *J. Imag. Sci. Technol.* 46.5 (2002), pp. 398–408.

[16] E Kim and J Baek. "Numerical stuyd on the effects of non-dimensional parameters on drop-on-demand droplet formation dynamics and printability range in the up-scaled model". *Phys. Fluids* 24.8 (2012), p. 082103.

[17] A van der Bos, M-J van der Meulen, T Driessen, M van den Berg, H Reinten, H Wijshoff, M Versluis, and D Lohse. "Velocity profile inside piezoacoustic inkjet droplets in flight: comparison between experiment and numerical simulation". *Phys. Rev. Appl.* 1 (2014), p. 014004. DOI: 10.1103/PhysRevApplied.1.014004.

[18] A B Aqeel, M Mohasan, P Lv, Y Yang, and H Duan. "Effects of nozzle and fluid properties on the drop formation dynamics in a drop-on-demand inkjet printing". *Applied Mathematics and Mechanics* 40 (2019), pp. 1239 –1254. DOI: 10.1007/s10483-019-2514-7.

[19] J Wang, J Huang, and J Zhang. "A method for calculating the critical velocity of microddroplets produced by circular nozzles". *3D Printing and Additive Manufacturing* 7.6 (2020), pp. 338–346. DOI: 10.1089/3dp.2019.0111.

[20] J Roenby, H Bredmose, and H Jasak. "A computational method for sharp interface advection". *Royal Society Open Science* 3 (2016), p. 160405. DOI: 10.1098/rsos.160405.

[21] I Gamet, M Scala, J Roenby, H Scheufler, and J-L Pierson. "Validation of volume-of-fluid OpenFOAM(R) isoAdve;ctor solvers using single bubble benchmarks". *Computers and Fluids* 213 (2020), p. 104722. DOI: 10.1016/j.compfluid.2020.104722.

[22] J E Fromm. "Numerical calculation of the fluid dynamics of drop-on-demand jets". *IBM J. Res. Develop.* 28 (1984), pp. 322–333. DOI: 10.1147/rd.283.0322.

[23] D Gerlach, G Biswas, F Durst, and V Kolobraric. "Ouasi-static bubble formation on submerged orifices". *Int. J. Heat Mass Transfer* 48.2 (2005), pp. 425–438. DOI: 10.1016/j.ijheatmasstransfer.2004.09.002.

[24] J Q Feng. "A computational study of bubble formation from an orifice submerged in liquid with constant gas flow". *J. Fluids Eng.* 148.1 (2026), p. 011404. DOI: 10.1115/1.4069163.

[25] J Q Feng. “Reducing bubble size detached from thin-wall needles submerged in liquids with pulsating gas flows”. *Transport Phenomena* 1.2 (2026), p. 20260064. DOI: 10.1515/tp-2026-0064.

[26] H Dong, W W Carr, and J F Morris. “Visualization of drop-on-demand inkjet: drop formation and deposition”. *Rev. Sci. Instru.* 77 (2006), p. 085101. DOI: 10.1063/1.2234853.

[27] J Eggers. “Universal pinching of 3d axisymmetric free-surface flow”. *Phys. Rev. Lett.* 71.21 (1993), pp. 3458–3460. DOI: 10.1103/PhysRevLett.71.3458.

[28] A U Chen, P K Notz, and O A Basaran. “Computational and experimental analysis of pinch-off and scaling”. *Phys. Rev. Lett.* 88 (2002), p. 174501. DOI: 10.1103/PhysRevLett.88.174501.

[29] P K Notz and O A Basaran. “Dynamics and breakup of a contracting liquid filament”. *J. Fluid Mech.* 512 (2004), pp. 223–256. DOI: 10.1017/S0022112004009759.

[30] A A Castrejon-Pita, J R Castrejon-Pita, and I M Hutchings. “The breakup of liquid filaments”. *Phys. Rev. Lett.* 108 (2012), p. 074506. DOI: 10.1103/PhysRevLett.108.074506.

[31] C R Anthony, H Wee, V Garg, S S Thete, P M Kamat, B Wagoner, E D Wilkes P K Notz, A U Chen, R Suryo, K Sambath, J C Panditaratne, Y-C Liao, and O A Basaran. “Sharp interface methods for simulation and analysis of free surface flows with singularities: breakup and coalescence”. *Annu. Rev. Fluid Mech.* 55 (2023), pp. 707–747. DOI: 10.1146/annurev-fluid-120720-014714.

[32] G H McKinley and M Renardy. “Wolfgang von Ohnesorge”. *Phys. Fluids* 23.12 (2011), p. 127101. DOI: 10.1063/1.3663616.

[33] D Jang, D Kim, and J Moon. “Influence of fluid physical properties on ink-jet printability”. *Langmuir* 25 (2009), pp. 2629–2635. DOI: 10.1021/la900059m.

[34] Y Liu and B Derby. “Experimental study of the parameters for stable drop-on-demand inkjet performance”. *Phys. Fluids* 31 (2019), p. 032004. DOI: 10.1063/1.5085868.

[35] L S Klyachko. “Heating and ventilation”. *USSR Journal Otopl. i Ventil.* No. 4 (1934).

[36] J S Serafini. *Impingement of water droplets on wedges and double-wedg airfoils at supersonic speeds*. Tech. rep. NASA-TP-1159. NASA Lewis Flight Propulsion Laboratory, 1954.

[37] N A Fuchs. *The Mechanics of Aerosols*. New York: Dover, 1964.

[38] D Barnett and M McDonald. “Evaluation and reduction of elevated height printing defects”. Vol. 30. 2014, pp. 38 –43. DOI: 10.2352/ISSN.2169-4451.2014.30.1.art00012.1.

[39] O Oktavianty, Y Ishii, S Haruyama, T Kyoutani, Z Darmawan, and S E Swara. "Controlling droplet behaviour an quality of DoD inkjet printer by designing actuation waveform for multi-drop method". Vol. 1034. Malang, Indonesia, 2021, p. 012091. DOI: 10.1088/1757-899X/1034/1/012091.

[40] T D Blake and K J Ruschak. "Wetting: Static and Dynamic Contact Lines". *Liquid Film Coating—Scientific Principles and Their Technological Implications*. Ed. by S F Kistler and P M Schweizer. Dordrecht, the Netherlands: Chapman & Hall, 1997, pp. 62–97.

[41] Y Chen, R Mertz, and R Kulenovic. "Numerical simulation of bubble formulation on orifice plates with a moving contact line". *Int J Multiphase Flow* 35.1 (2009), pp. 66–77. DOI: 10.1016/j.ijmultiphaseflow.2008.07.007.